



Optimal echo times for quantitative susceptibility mapping: A test-retest study on basal ganglia and subcortical brain nuclei

Valentina Bordin^{a,*}, Alice Pirastru^{a,b}, Niels Bergsland^{b,c}, Marta Cazzoli^b, Giuseppe Baselli^a, Francesca Baglio^b

^a Department of Electronics, Information and Bioengineering, Politecnico di Milano, Milan, Italy

^b IRCCS Fondazione Don Carlo Gnocchi ONLUS, Milan, Italy

^c Department of Neurology, Buffalo Neuroimaging Analysis Center, School of Medicine and Biomedical Sciences, University at Buffalo, State University of New York, Buffalo, NY, United States



ARTICLE INFO

Keywords:

Magnetic resonance imaging
Quantitative susceptibility mapping
Repeatability
Basal ganglia
Subcortical brain nuclei
Longitudinal study

ABSTRACT

Quantitative Susceptibility Mapping (QSM) is a recent MRI-technique able to quantify the bulk magnetic susceptibility of myelin, iron, and calcium in the brain. Its variability across different acquisition parameters has prompted the need for standardisation across multiple centres and MRI vendors. However, a high level of agreement between repeated imaging acquisitions is equally important. With this study we aimed to assess the inter-scan repeatability of an optimised multi-echo GRE sequence in 28 healthy volunteers. We extracted and compared the susceptibility measures from the scan and rescan acquisitions across 7 bilateral brain regions (i.e., 14 regions of interest (ROIs)) relevant for neurodegeneration. Repeatability was first assessed while reconstructing QSM with a fixed number of echo times (i.e., 8). Excellent inter-scan repeatability was found for putamen, globus pallidus and caudate nucleus, while good performance characterised the remaining structures. An increased variability was instead noted for small ROIs like red nucleus and substantia nigra. Secondly, we assessed the impact exerted on repeatability by the number of echoes used to derive QSM maps. Results were impacted by this parameter, especially in smaller regions. Larger brain structures, on the other hand, showed more consistent performance. Nevertheless, with either 8 or 7 echoes we managed to obtain good inter-scan repeatability on almost all ROIs. These findings indicate that the designed acquisition/reconstruction protocol has wide applicability, particularly in clinical or research settings involving longitudinal acquisitions (e.g. rehabilitation studies).

1. Introduction

Quantitative Susceptibility Mapping (QSM) is an advanced Magnetic Resonance Imaging (MRI) technique providing quantitative measurements of the bulk magnetic susceptibility characterizing biological tissues (Reichenbach, 2012; de Rochefort et al., 2010; Li and Leigh, 2004; Wang and Liu, 2015). The method exploits the phase signal of Gradient Recalled Echo (GRE) sequences, which is typically discarded in conventional image reconstruction procedures despite retaining useful information. The phase grows proportionally with disturbances in the magnetic field caused by the interaction of paramagnetic and diamagnetic molecules – present within the human body – with the static magnetic field of the MRI. These elements play a crucial role in determining tissue susceptibility. Thus, by solving an inverse ill-posed problem that begins with the phase content (i.e., field variations), it becomes possible to accurately estimate this property.

Given its physical principles, QSM is highly sensitive to different brain metabolites including myelin, iron, calcium, and blood compounds (Haacke et al., 2015; Feng et al., 2018). Hence, it holds great potential for diagnosing and monitoring a wide range of neurological diseases. Various studies have indicated QSM as an effective tool for analysing the process of demyelination (Huang et al., 2022; Argyridis et al., 2014; Wharton and Bowtell, 2015) and for detecting white matter lesions that are frequent in multiple sclerosis patients (Wisnieff et al., 2015). In addition, QSM has proved to be highly sensitive to increased iron concentration as compared to traditional R2* relaxometry (Du et al., 2016; Murakami et al., 2015). This encouraged its applications in a variety of fields, including the detection of iron accumulation in deep cerebral nuclei. Similar findings are often linked to the presence of neurodegenerative conditions such as Parkinson's disease (Langkammer et al., 2016) and Alzheimer's disease (Du et al., 2018; Acosta-Cabronero et al., 2013).

* Corresponding author at: Department of Electronics, Information and Bioengineering, Politecnico di Milano, Via Camillo Golgi 39, 20133 Milan, Italy
E-mail address: valentina.bordin@polimi.it (V. Bordin).

Due to its clinical relevance and quantitative nature, QSM appears as an ideal candidate for the long-term assessment of neurological conditions in which altered homeostasis may have a role. However, the degree of variability revealed by susceptibility maps when derived from MRI scans using different magnetic field strength and acquisition parameters has raised concerns regarding its ability to provide reliable findings in longitudinal follow-ups. For example, it has been reported that 7T MRI scanners allow equivalent image quality with respect to 3T ones in half of the scan time (Spincemaille et al., 2020). This may be ascribed to an increased phase contrast and signal-to-noise ratio (SNR) of the magnitude images at 7T (Emmerich et al., 2021). Another study investigating QSM reproducibility suggested that, in multi-centric scenarios where different MRI field strength are used, the choice of acquisition parameters such as the time of echo (i.e., TE) is crucial to derive similar results (Lancione et al., 2019). The influence of TE has further been stressed in other studies (Sood et al., 2017; Cronin et al., 2017; Naji et al., 2022). The white matter and deep gray matter nuclei have displayed a non-linear trend of variation, as a function of TE, in the computed susceptibility values (Fan et al., 2020). Besides TE, the spatial resolution (in terms of both slice thickness and spacing) (Zhou et al., 2017; Karsa et al., 2019), brain coverage (in terms of % field of view) (Karsa et al., 2019; Elkady et al., 2016) and head orientation with respect to the B_0 field (Lancione et al., 2017) have also been indicated as possible factors contributing to increased differences in the final QSM estimates.

This major and complex variability has prompted numerous evaluations targeting the reproducibility of QSM across different sites (Spincemaille et al., 2020; Ippoliti et al., 2018; Hinoda et al., 2015). Several studies have also attempted to harmonise the imaging acquisition protocol for QSM, prior to assessing reproducibility (Rua et al., 2020; Clarke et al., 2020; Voelker et al., 2021). Among these, the RIN – Neuroimaging Network (Nigri et al., 2022), has recently harmonized and tested the multi-centre/multi-vendor reliability of a multi-echo GRE sequence suited for QSM (Lancione et al., 2022). They found promising results on both subcortical (i.e., caudate nucleus, putamen, globus pallidus and hippocampus) and cortical grey matter regions (i.e., cuneus, precuneus, precentral gyrus and superior frontal gyrus).

However, not only reproducibility but also a high level of agreement between measures extracted from repeated MRI acquisitions is fundamental to ensure the collection of unbiased datasets and to allow the potential development/implementation of quantitative biomarkers (Salluzzi et al., 2022). Moreover, repeatability has to be considered with respect to the imaging acquisition parameters and specifically accounting for the TE effect. To this aim, 28 young and healthy volunteers were enrolled in this study and acquired twice using a multi-echo GRE sequence (Lancione et al., 2022). Two levels of analysis (i.e., ROI-based and voxel-wise) were implemented to assess the repeatability of QSM and its dependence on the number of echoes. Results were evaluated over 7 regions of interest (ROIs) comprising basal ganglia and subcortical brain nuclei, chosen as relevant for neurodegeneration.

2. Methods

2.1. Subjects

Twenty-eight young volunteers (see Table 1 for demographic details) without any history of neurological or psychiatric diseases, according to clinical interview, underwent an MRI scanning session at IRCCS Fondazione Don Gnocchi ONLUS in Milan. The study was approved by the local ethics committee and carried out according to the Declaration of Helsinki. Informed written consent was obtained from all participants.

2.2. MRI acquisition

The imaging protocol comprised two sequences acquired on a 3T Siemens MAGNETOM Prisma scanner (Siemens Healthineers, Erlan-

Table 1
Demographics of the study population.

Subjects	Number	28
Age (years)	Mean	28.8
	Standard Deviation	3.96
	Range (min – max)	22.9–38.1
Sex	M	14
	F	14

gen Germany), equipped with a 64-channel head/neck coil: (i) a flow-compensated 3D multi-echo GRE sequence used to derive both magnitude and phase volumes relative to the susceptibility mapping; acquisition parameters were set according to the protocol defined by the RIN (Nigri et al., 2022) for Siemens vendor: number of echoes = 8, $\Delta TE = 5.6$ ms, first TE = 5.6 ms, TR = 51 ms, flip angle = 18° , voxel size = $1 \times 1 \times 1$ mm³, FoV = 224×224 mm², slices per slab = 144, readout mode = bipolar, acquisition time = 8.45 min; acquisition were carried out using a pure axial orientation; (ii) a high resolution 3D magnetization prepared GRE (MPRAGE) sequence used as anatomical reference and acquired with the following parameters: voxel size = $0.8 \times 0.8 \times 0.8$ mm³, TR = 2300 ms, TE = 3.1 ms, FOV = 256×240 mm², slices per slab = 224, acquisition time = 6.21 min.

In order to test the inter-scan repeatability, every subject repeated the QSM acquisition twice with an interscan interval of 10 minutes and bed repositioning (i.e., subjects exited and re-entered the scanning bed, while it underwent a complete retraction and repositioning).

2.3. QSM processing

For the entire dataset, we reconstructed QSM maps using MATLAB 2021a (MathWorks, Natick, MA, USA). Both magnitude and phase volumes from the 3D GRE sequence were used as inputs for the Morphology Enabled Dipole Inversion (MEDI) Toolbox developed by the Cornell MRI Research Lab (Cornell MRI Research Group, 2020). Minor changes to the original code enabled to spatially unwrap the raw phase images acquired at every echo using a Laplacian based algorithm (Li et al., 2011). The subsequent step of background field removal was carried out by means of Projection onto Dipole Fields (PDF). At this point, the processed phase was combined with the corresponding echo magnitude to derive a complex GRE signal, for all the available echoes. The obtained results were then pooled using a complex nonlinear fitting to estimate the local magnetic field of tissues. To perform the multi-echo combination step a modified version of the original `Fit_ppm_complex` function (Cornell MRI Research Group, 2020) (i.e., `Fit_ppm_complex_bipolar`) was used to account for the bipolar readout mode of our data. Finally, susceptibility values were estimated through the Morphology Enabled Dipole Inversion algorithm with automatic uniform cerebrospinal fluid zero referencing (MEDI+0) (Liu et al., 2018). The final QSM maps were expressed in parts per billion (ppb).

All the available echoes were initially used to derive QSM maps, for both the scan and rescan acquisitions (i.e., SC1 and SC2). The same procedure was then repeated using a decreasing number of echoes times (i.e., nTEs), (i.e., late nTEs were removed thus decreasing the overall range of echo times) as we looked for potential differences in the inter-scan repeatability results (see the “2.4. Data analysis” section for further details). We completed the analysis as we reached the minimum nTEs (i.e., 3) needed to perform the multi-echo complex linear fitting with `Fit_ppm_complex_bipolar` (Cornell MRI Research Group, 2020).

2.4. Data analysis

Our analysis comprised two different steps to evaluate the inter-scan repeatability of the final QSM maps: i) a ROI-based assessment

performed in the native subject space. The ROI-based analysis was performed on QSM maps reconstructed using all the available echoes (i.e., nTEs = 8). The rationale was to investigate the level of across scans repeatability characterising individual ROIs at a fixed nTEs; ii) both a voxel-wise analysis – carried out after normalizing the QSM maps to the standard Montreal Neurological Institute (MNI) template – and a ROI-based assessment – performed in the native subject space – were used to explore the dependence between the level of inter-scan repeatability characterising individual ROIs and the nTEs used to derive QSM reconstructions. The rationale behind this choice lies with the variability introduced by this acquisition parameter on the final susceptibility estimates. The TE-dependency is non-linear and has revealed different patterns across different brain nuclei (Sood et al., 2017; Cronin et al., 2017). Most importantly, TE has been shown to affect the multi-centre reproducibility of QSM across the whole brain (Lancione et al., 2019). Therefore, we aimed to assess whether a similar impact was present on the inter-scan repeatability of basal ganglia and subcortical brain nuclei.

2.4.1. Across scans repeatability

ROI-based analysis: in each subject, 7 brain nuclei were bilaterally segmented, for a total of 14 ROIs that were analysed separately. Five nuclei were segmented from the MPRAGE scan – thalamus (THL), putamen (PUT), globus pallidus (GP), amygdala (AMG), caudate nucleus (CN) – using the FSL 6.0 toolbox FIRST (Patenaude et al., 2011). Then, the derived masks were linearly registered to the first echo magnitude of the QSM sequence, using the FSL FLIRT toolbox (Jenkinson and Smith, 2001) (12 degrees of freedom). Conversely, substantia nigra (SN) and red nucleus (RN), were derived through a direct registration from the Edlow brain atlas (Snider et al., 2019) (i.e., MNI space $1 \times 1 \times 1 \text{ mm}^2$) to the QSM space. This was obtained by combining the following matrices with the ANTs toolbox (<http://stnava.github.io/ANTs/>): (i) the original MPRAGE to QSM transformation matrix; (ii) the inverse of the non-linear transformation matrix derived from the MPRAGE to MNI non-linear registration. Structures from the right and left hemisphere (i.e., RH and LH) were isolated and eroded through a 2D kernel (i.e., box of $3 \times 3 \times 1$ voxels), to obtain conservative masks. In addition, the RN underwent manual refinements to best fit the anatomical contours that can be well-identified on QSM data, according to the guidelines reported in Liu et al. (2016). Finally, for each of the considered ROIs, the binary mask was applied to the QSM reconstruction relative to SC1 and SC2 and, for both cases, mean values were extracted. The obtained results (i.e., the ROI means) were combined across the entire dataset and compared between SC1 and SC2 using several metrics to provide a detailed assessment of the inter-scan repeatability characterising different brain nuclei. At first, we calculated the intra-class correlation coefficient (ICC) between the repeated measures to obtain a quantitative evaluation of their agreement. We used the statistical package SPSS version 27 (Armonk, NY: IBM Corp). A single-rating, absolute agreement, two ways mixed-effect model was adopted (McGraw and Wong, 1996, Koo and Li, 2016). According to Koo and Li (2016), ICC values lower than 0.5 indicate poor repeatability, values between 0.5 and 0.75 indicate moderate repeatability, values between 0.75 and 0.9 indicate good reliability, and values greater than 0.90 indicate excellent reliability. The assessment was further carried out by computing the linear regression between ROI QSM values extracted from SC1 and SC2. The angular coefficient and the intercept of the linear fit were reported for every ROI alongside the Pearson's correlation coefficient. Similarly, Bland-Altman plots were derived for every ROI to display the mean difference between SC1 and SC2, alongside the 95% confidence interval (CI – i.e., 1.96 times the standard deviation). As previously stated, the present analysis was performed on QSM reconstructions obtained using all the available echoes (i.e., nTEs = 8).

2.4.2. TE dependence

Voxel-wise analysis: for every subject, the final QSM reconstructions were normalized to the standard MNI space ($1 \times 1 \times 1 \text{ mm}^2$) by

combining with the ANTs toolbox (<http://stnava.github.io/ANTs/>): (i) the inverse of the original MPRAGE to QSM transformation matrix; (ii) the transformation matrix derived from the MPRAGE to MNI non-linear registration. At this point, the same seven brain nuclei considered for the ROI-based analysis were isolated from the Harvard Oxford atlas (Goldstein et al., 2007; Makris et al., 2006; Frazier et al., 2005; Desikan et al., 2006), eroded through a 2 mm spherical kernel and finally re-combined to obtain a single 3D mask (i.e., a single volume comprising all ROIs). Then, for both SC1 and SC2, we merged the QSM maps relative to all participants into a 4D file. The obtained results (i.e., one 4D file for SC1 and one 4D file for SC2) were eventually compared using the *fmrli* MATLAB toolbox (Fröhner et al., 2019). The tool, originally designed to assess the reliability and similarity of fMRI data in the present work, was exploited to calculate the voxel-wise ICC between the SC1 and SC2 measures constrained to the anatomical regions underlying the binary nuclei mask. Even in this case, a single-rating, absolute agreement, two ways mixed-effect model was adopted. Results were provided in the form of a 3D volume containing a single ICC value for every voxel belonging to the binary nuclei mask. The analysis was repeated for every QSM reconstruction obtained using a decreasing number of echoes ranging from 8 to 3. Finally, ICC values found within the mask were extracted at different nTEs and compared. The mean, first quartile, third quartile and minimum values of each distribution were discussed, along with the percentage volume of the binary mask containing ICC values higher than 0.75. We determined the number of echoes to be sufficient if the average of the whole mask scored 0.75 or higher, since ICC values in ranging from 0.75 to 1 indicate good to excellent inter-scan agreement (Koo and Li, 2016).

ROI-based analysis: we repeated the across scan repeatability analysis (see the “2.4.1. Across scans repeatability” section for further details) – initially performed on all the available echoes (i.e., nTEs = 8) – using progressively decreasing nTEs. In addition, for every ROI, we specifically investigated the dependence of ICC values with respect to the different nTEs used to derive QSM maps. This allowed us to explore any potential change in the level of repeatability characterising the mean susceptibility of different brain nuclei when using a nTEs lower than 8. Even in this case, we considered as indicators of good repeatability ICC values greater than 0.75 (Koo and Li, 2016). The TE-dependence of the inter-scan repeatability was further explored at nTEs higher than 8, as we acquired an additional scan-rescan subject using a maximum echo time of 80 ms and compared its SC1 and SC2 mean QSM values across echoes (see the *Supplementary Materials* for details).

3. Results

3.1. Across scans repeatability

ROI-based analysis. The average volume of all ROIs, calculated across the entire population, is reported in Table 2. As for the susceptibility maps obtained using 8 nTEs, the box plots of the ROI QSM values relative to SC1 and SC2 are displayed in Fig. 1. The right (Fig. 1, Panel A) and the left (Fig. 1, Panel B) structures are shown separately, for a total of 14 ROIs. The mean and standard deviation values relevant to all distributions are reported in the *Supplementary Materials* whereas the ICC computed between SC1 and SC2 are reported in Table 3. Overall, results indicated that no structure other than the RN_{RH} was characterised by a level of inter-scan repeatability lower than good (ICC = 0.735 for RN_{RH} and ICC > 0.75 for all the remaining structures). Additionally, for both brain hemispheres, the following structures displayed an ICC > 0.90, indicating excellent repeatability: PUT (RH: ICC = 0.960; LH: ICC = 0.913), GP (RH: ICC = 0.956; LH: ICC = 0.958) and CN (RH: ICC = 0.902; LH: ICC = 0.912). The orthogonal linear fit between SC1 and SC2 is reported in Fig. 2 for every ROI separately for right (Fig. 2, Panel A) and left (Fig. 2, Panel B) brain nuclei. Results confirmed a good correspondence between the repeated ROI QSM values. The angular coefficient (m) of the computed regressions was high (ideal value: m = 1),

Table 2

Average volume of brain nuclei segmented in native subject space, separated by right and left brain hemisphere. Results were evaluated on the full sample.

		THL	PUT	GP	AMG	CN	SN	RN
Volume (mm ³ /number of voxels)	RIGHT BRAIN HEMISPHERE	6041.9	2935	954.6	664.1	1946.2	66.3	66.8
	LEFT BRAIN HEMISPHERE	6147.7	2895.8	922.0	631.6	1848.7	58.2	59.7

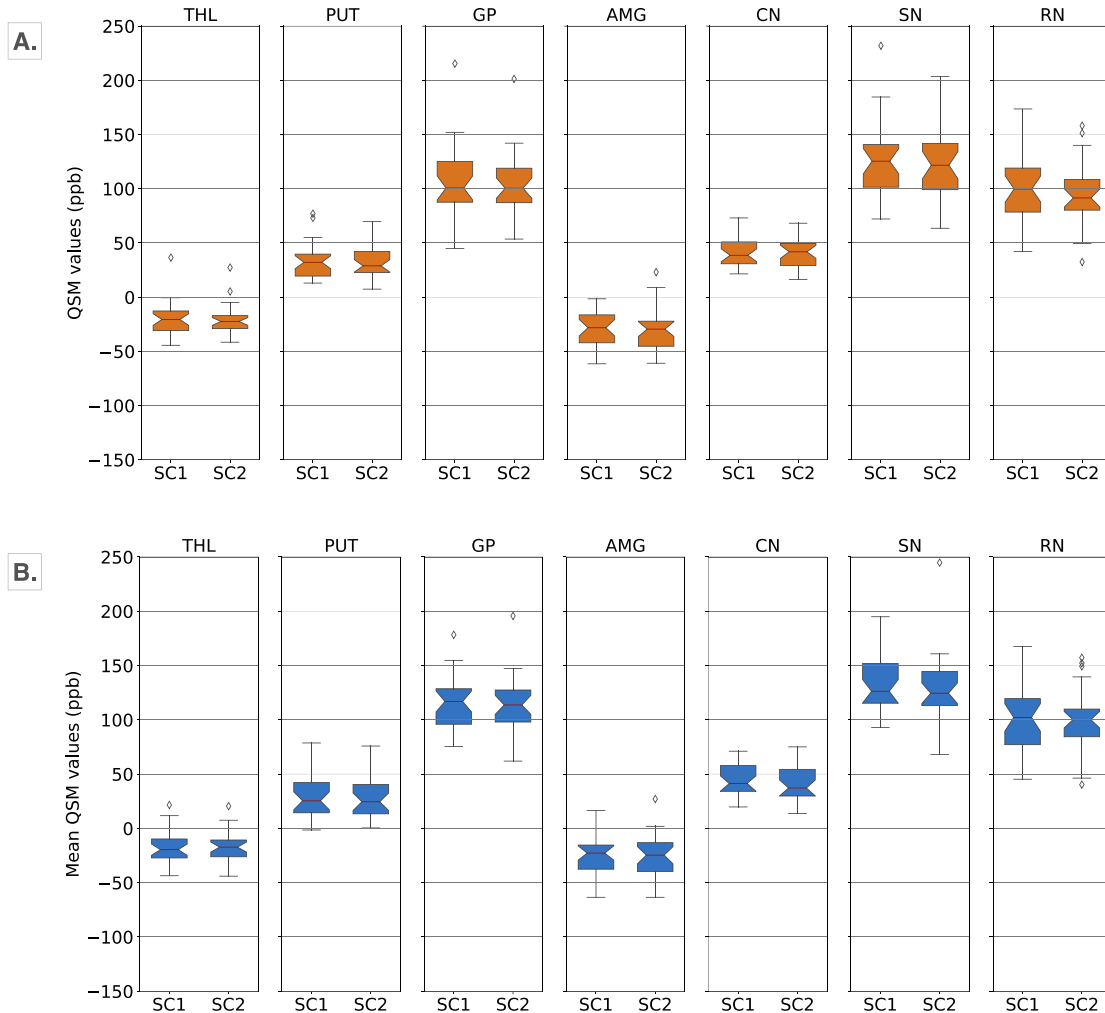


Fig. 1. Boxplots of the ROI QSM in the scan (SC1) and the rescans (SC2) acquisition (specified on the x-axis) for brain nuclei of the right (A) and left (B) brain hemisphere. Results were evaluated on the full sample, after reconstructing QSM with 8 nTEs.

Table 3

Intra-class correlation coefficient (ICC) between the QSM distributions relative to the scan (SC1) and rescans (SC2) acquisition for brain nuclei of the right and left brain hemisphere. Results were evaluated on the full sample, after reconstructing QSM with 8 nTEs.

		THL	PUT	GP	AMG	CN	SN	RN
RIGHT BRAIN HEMISPHERE	ICC	0.835	0.956	0.96	0.787	0.902	0.826	0.735*
LEFT BRAIN HEMISPHERE	ICC	0.824	0.958	0.913	0.870	0.912	0.766	0.834

* ICC < 0.75.

ranging from 0.874 to 0.993, for the following structures: PUT (both RH and LH), GP (both RH and LH), AMG (both RH and LH), CN (both RH and LH) and SN_{LH}. Even if lower values were found for THL (both RH and LH), SN_{RH} and RN (both RH and LH), values never dropped below 0.7. The only exception was represented by the RN_{RH} (m = 0.648). Good inter-scan repeatability was further indicated by the small regres-

sion intercepts characterising all the investigated nuclei (range 0.403–9.864). The presence of a minor offset was instead suggested by the higher values obtained for SN_{RH} (b = 29.184) and RN (RH: b = 29.650; LH: b = 19.571). The Pearson’s correlation coefficients gave good result for every structure (range 0.777–0.972).

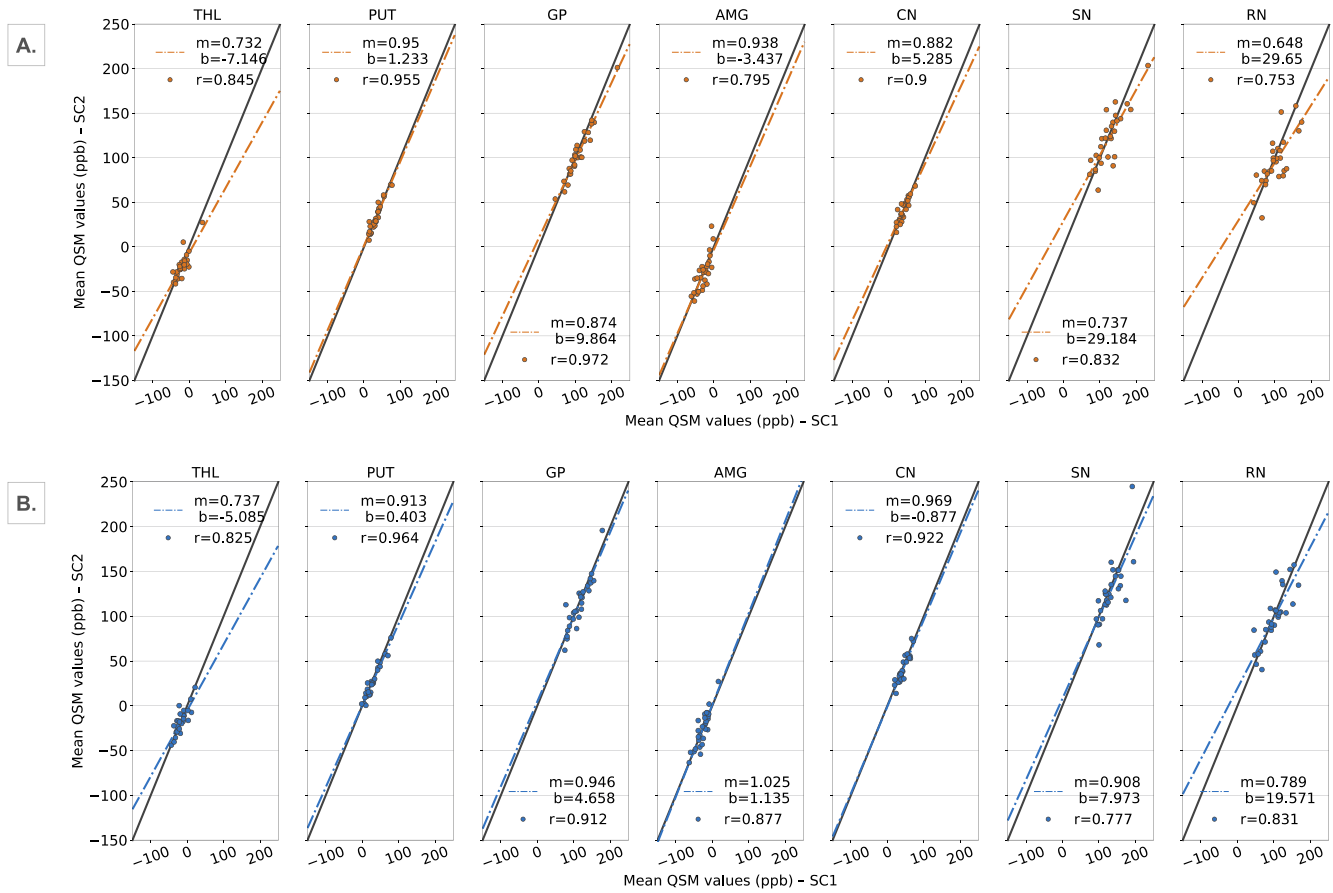


Fig. 2. Scatterplot of the ROI QSM in the scan (SC1) and the rescan (SC2) acquisition for brain nuclei of the right (A) and left (B) brain hemisphere. The regression fits are displayed with dash-dotted coloured lines (orange and blue for the right and left brain nuclei, respectively), while the ideal fits are represented with black solid lines. The regression slopes and intercepts are indicated as m and b , respectively. The Pearson's correlation coefficient is indicated as r . Results were evaluated on the full sample, after reconstructing QSM with 8 nTEs. (For interpretation of the references to colour in this figure legend, the reader is referred to the web version of this article.)

Table 4

Descriptive statistic for the SC1–SC2 voxel-wise ICC values obtained at decreasing nTEs over a binary mask comprising all ROIs (see Fig. 4).

	8 nTEs	7 nTEs	6 nTEs	5 nTEs	4 nTEs	3 nTEs
Mean \pm standard deviation	0.762 \pm 0.120	0.756 \pm 0.127	0.735 \pm 0.138	0.717 \pm 0.147	0.634 \pm 0.181	0.589 \pm 0.186
First quartile	0.694	0.693	0.668	0.644	0.532	0.471
Third quartile	0.851	0.849	0.838	0.824	0.768	0.731
Min–Max range	0.197–0.964	0.070–0.960	–0.018–0.945	–0.070–0.944	–0.410–0.939	–0.383–0.941
% volume with ICC > 0.75	61.27%	60.63%	55.08%	49.91%	30.18%	20.85%

The Bland-Altman analysis, plots are reported in Fig. 3 for every ROI, separately for right (Fig. 3, Panel A) and left (Fig. 3, Panel B) structures. The mean difference between SC1 and SC2 yielded low values (range -0.51 – 3.83 ppb) for almost all nuclei. A slight bias was instead revealed by the RN_{RH} (mean difference 6.29 ppb) and SN_{LH} (mean difference 4.22 ppb). Similar results were found for the 95% CI. Broad intervals were obtained only for SN (RH: CI = 41.18; LH: CI = 43.49) and RN (RH: CI = 47.71; LH: CI = 37.62).

3.2. TE dependence

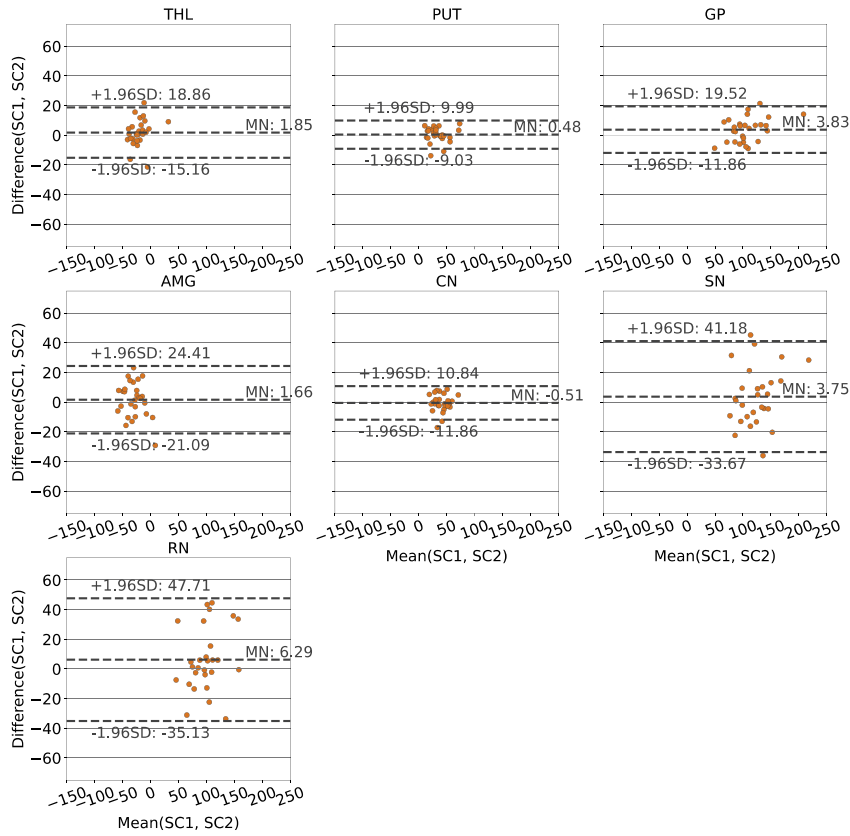
Voxel-wise analysis. As displayed in Fig. 4, we extracted and compared the SC1–SC2 voxel-wise ICC obtained at every nTEs over a binary mask comprising all ROIs. Results showed a decreasing trend in the inter-scan agreement when passing from 8 to 3 nTEs. This was supported by a reduction in the mean, first quartile and third quartile values

that characterise ICC distributions at small nTEs (see Table 4). In addition, when using less than 7 echoes the ICC metric provided negative scores whose amount increased at lower nTEs. Eventually, when considering the limit of 0.75 as criterion for determining good repeatability (Koo and Li, 2016), it can be observed that the only reconstructions with a mean ICC higher than the threshold over all ROIs are obtained using 7 or 8 nTEs.

These two nTEs are also the ones maximizing the percentage volume of the binary mask for which we have ICC > 0.75 (8 nTEs: 61.27%; 7 nTEs: 60.63%), as is clearly visible from the example shown in Fig. 5.

ROI-based analysis. Results from all the metrics used to evaluate the across scan repeatability of different ROIs when using nTEs values progressively lower than 8 (see the “2.4.1. Across scans repeatability” section for further details) are reported in the *Supplementary Materials*. However, the nTEs-evolution of ICC values is displayed in Fig. 6 for every ROI, separately for right (Fig. 6, Panel A) and left structures (Fig. 6,

A.



B.

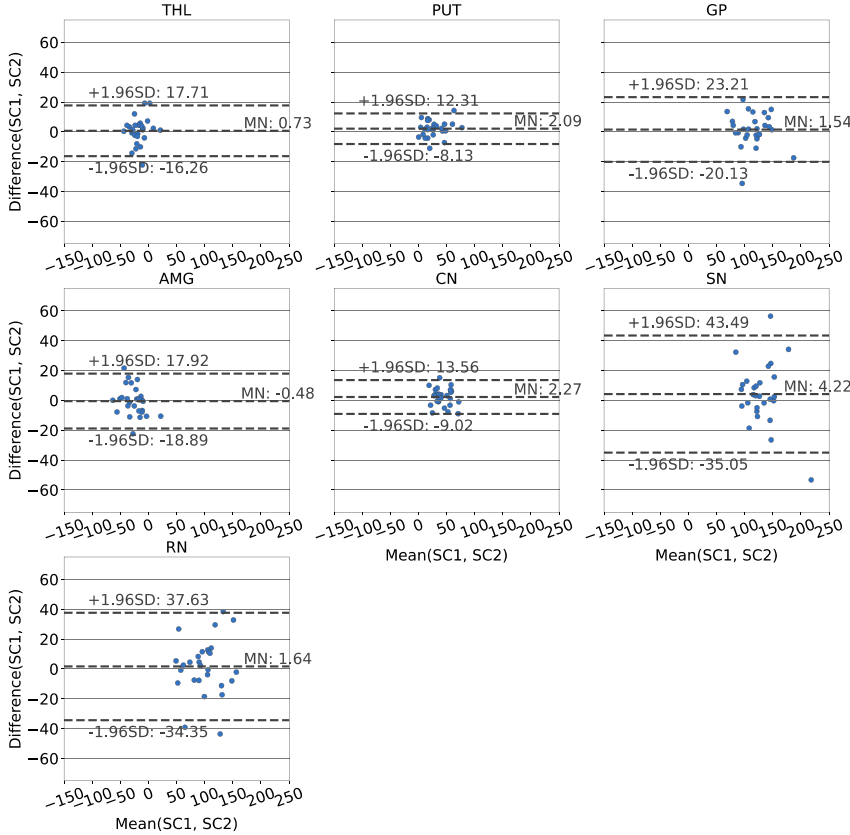


Fig. 3. Bland-Altman plot of the ROI QSM in the scan (SC1) and the rescans (SC2) acquisition for brain nuclei of the right (A) and left (B) brain hemisphere. The mean difference between SC1 and SC2 are highlighted with dashed lines alongside the confidence interval (i.e., 1.96 times the standard deviation (SD)). Results were evaluated on the full sample, after reconstructing QSM with 8 nTEs.

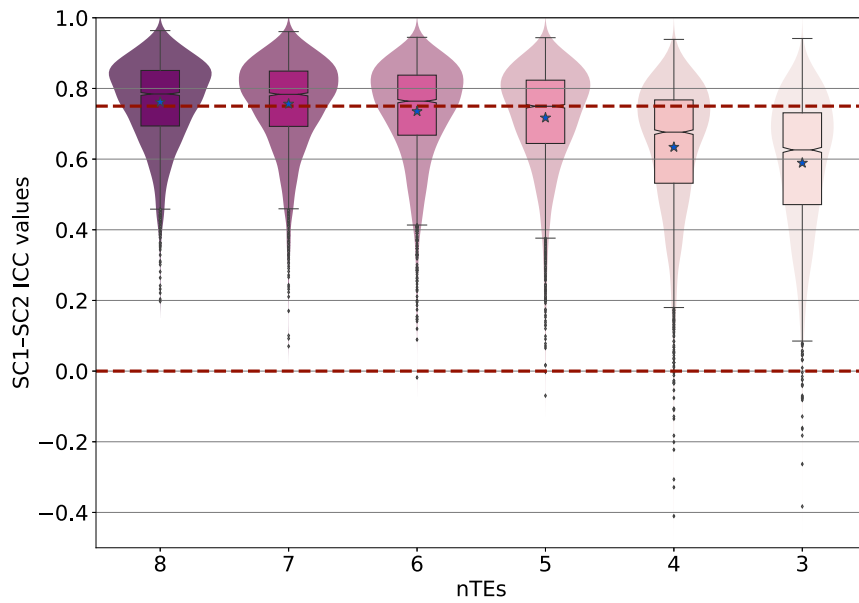


Fig. 4. Violin plots of the voxel-wise SC1–SC2 ICC values obtained over a binary mask comprising all ROIs at decreasing nTEs (each indicated by a fading shade of purple). The interquartile range and median value of each distribution is represented through a boxplot. Mean values are displayed by black stars. Two dashed red lines highlight the range of ICC values comprised between 0.0 and 0.75. Results were evaluated on the full sample. (For interpretation of the references to colour in this figure legend, the reader is referred to the web version of this article.)

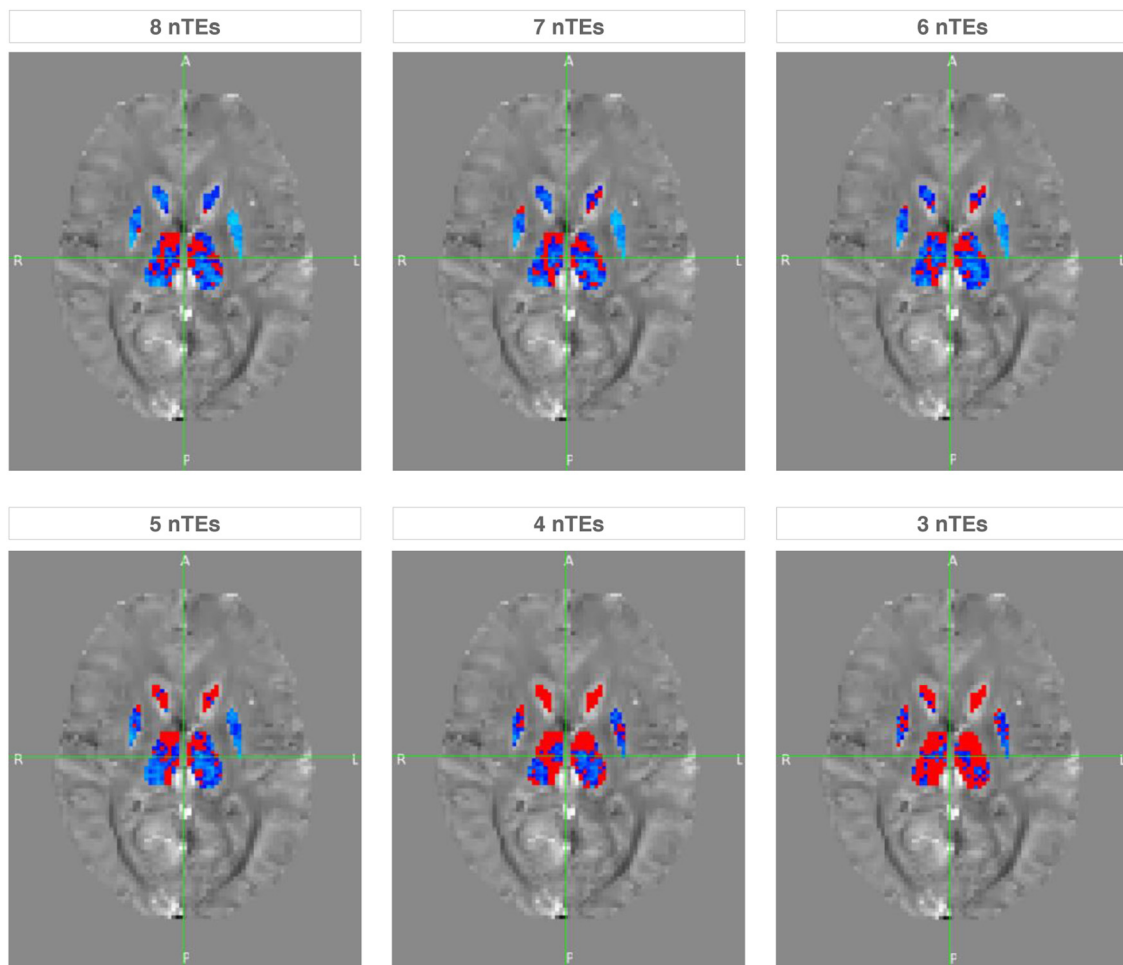


Fig. 5. Effect of the nTEs used to perform reconstructions on the level of voxel-wise inter-scan repeatability characterising QSM. ICC maps are shown relevant to slice $z = 40$ and in the MNI space: good ICC > 0.75 is displayed in blue, while poor ICC < 0.75 is displayed in red. The ICC maps are superimposed to the QSM of a single representative subject. (For interpretation of the references to colour in this figure legend, the reader is referred to the web version of this article.)

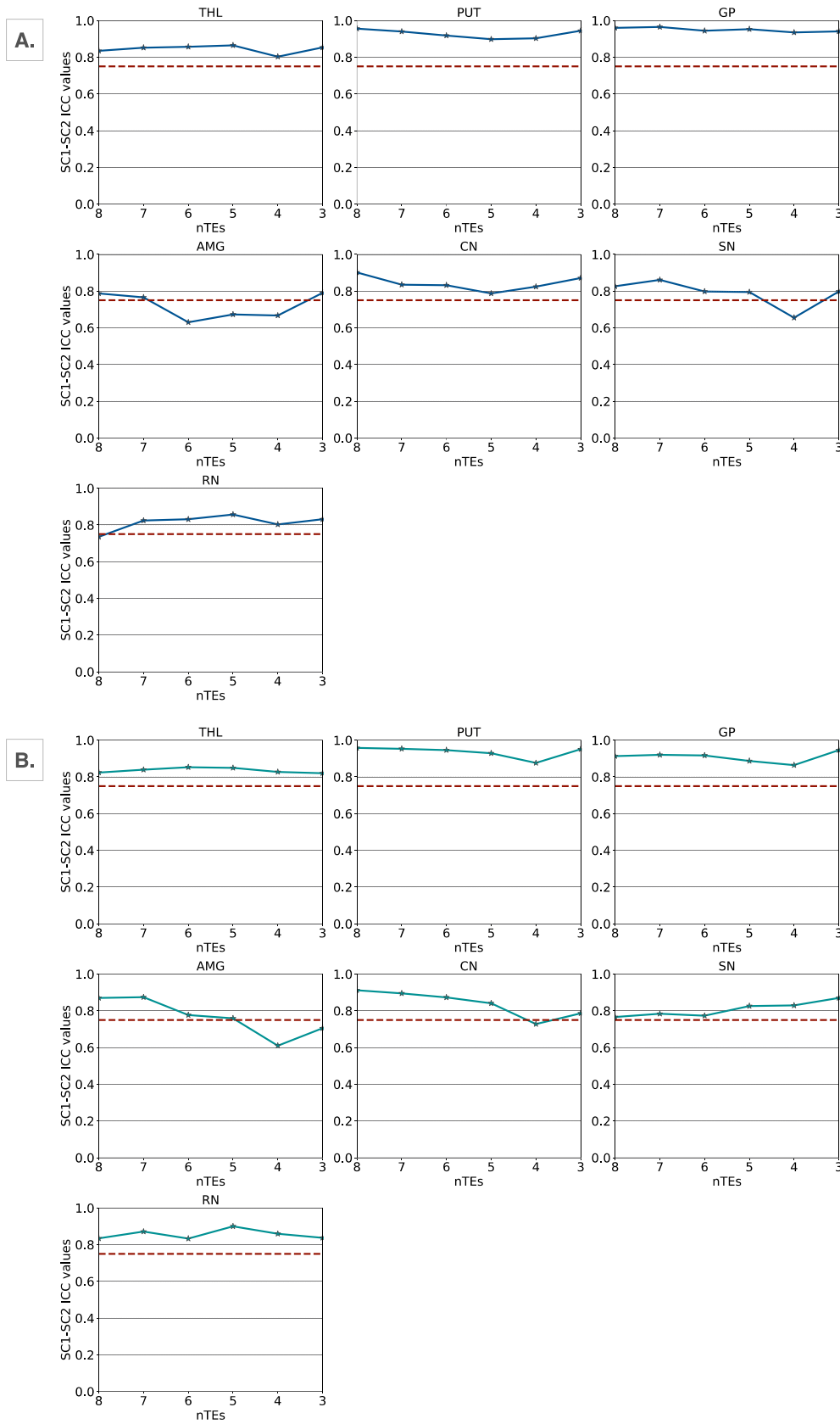


Fig. 6. Lineplot of the nTEs-evolution of the intra-class correlation coefficient (ICC) between ROI QSM in the scan (SC1) and the rescans (SC2) acquisition for brain nuclei of the right (A) and left (B) brain hemisphere. A dashed red line indicates the ICC threshold for good repeatability (i.e., ICC = 0.75). Results were evaluated on the full sample. (For interpretation of the references to colour in this figure legend, the reader is referred to the web version of this article.)

Panel B). Numerical values are reported in the *Supplementary Materials*. The structures displaying good inter-scan repeatability (i.e., ICC values above 0.75) for all nTEs were: PUT (both RH and LH), GP (both RH and LH) and THL (both RH and LH). A similar behaviour was also displayed by the CN, that showed a sole performance drop at nTEs = 4 (ICC = 0.728) in correspondence of the LH. Nevertheless, for both hemispheres the highest ICC values were obtained when using high nTEs (i.e., nTEs = 8) (RH: ICC = 0.902; LH: ICC = 0.912). A greater amount of variability was instead exhibited by the repeatability pattern of the AMG. This nucleus showed ICC values higher than 0.75 for nTEs = 8, 7, 6, 5 (in the RH) and for nTEs = 8, 7, 3 (in the LH). Lower performances were instead detected in correspondence of the remaining nTEs values. As for the SN, the LH was always characterised by ICC above 0.75, with slightly increased values as we move towards lower nTEs. The RH, on the other hand, showed a decrease in the ICC at nTEs = 4 (ICC = 0.655) and highest repeatability at nTEs = 7 (ICC = 0.861). Eventually, good performances were found for all nTEs for both RN_{RH} and RN_{LH}. The only exception was represented by nTEs = 8 for RN_{RH} (ICC = 0.735). The highest ICC was found at nTEs = 5 for both hemispheres.

4. Discussion

QSM is an imaging technique that could be favourably used to derive imaging biomarkers for several neurological conditions. In fact, it provides quantifiable measures of the magnetic susceptibility characterising brain tissues and helps monitoring subtle changes in their own composition. In this study, we explored the inter-scan repeatability of the QSM maps reconstructed using a flow-compensated 3D multi-echo GRE sequence (Lancione et al., 2022) within 14 regions of interest (ROIs) covering putamen (PUT), globus pallidus (GP), caudate nucleus (CN), thalamus, amygdala, red nucleus, and substantia nigra bilaterally. The inter-scan repeatability is of fundamental importance, especially in longitudinal MRI settings where patients' neurodegeneration patterns and their modifications have to be closely monitored over time for diagnostic and treatment purposes. However, the local reliability of susceptibility measures is still a matter of debate since QSM maps have displayed a great level of variability when derived according to different MRI setups (Spincemaille et al., 2020; Emmerich et al., 2021; Lancione et al., 2019; Sood et al., 2017; Cronin et al., 2017; Naji et al., 2022; Fan et al., 2020; Zhou et al., 2017; Karsa et al., 2019; Elkady et al., 2016). To address this issue, we implemented two different assessments while measuring the repeatability of QSM across a scan and rescan MRI acquisition: (i) first, a ROI-based analysis allowed to compare mean susceptibility values when QSM maps were reconstructed using a fixed number of echoes. Specifically, we used all the 8 available ones; (ii) second, a composite analysis – comprising both a voxel-wise and a ROI-based step – allowed to compare susceptibility values both across scans and along different echo times. Throughout the study, we used different metrics to evaluate results (see the “2.4. Data analysis” section for further details), the major one being represented by the intra-class correlation coefficient (ICC).

Using all the acquired 8 echoes in the ROI-based analysis, we observed excellent inter-scan repeatability in terms of ICC values (i.e., ICC > 0.90) for basal ganglia (PUT_{RH}: ICC = 0.956, PUT_{LH}: ICC = 0.958; GP_{RH}: ICC = 0.960, GP_{LH}: ICC = 0.913; CN_{RH}: ICC = 0.902, CN_{LH}: ICC = 0.912). This was further confirmed by a good linear regression fit (i.e., angular coefficient close to 1 and low intercept) between the repeated QSM estimates (m: ranging from 0.874 to 0.969; b: ranging from -0.877 to 9.864). Similarly, good results were obtained for the amygdala, though, with ICC values comprised between 0.75 and 0.90. A slightly lower repeatability was instead observed for the thalamus as highlighted by a decrease in the angular coefficient of the regression fit (RH: m = 0.732; LH: m = 0.737). This could be due to strong heterogeneity characterising this structure, which is organized in nuclear regions delimited by white matter trabeculae, each with a unique input-output connectivity pattern, gene expression and function (Roy et al.,

2022). However, it should be noted that, the ICC values between scans remained high (RH: ICC = 0.835; LH: ICC = 0.824), suggesting the local reliability of the current acquisition and reconstruction pipeline which seem suitable to longitudinally assess the susceptibility of thalamus. Additionally, our findings showed that the red nucleus and substantia nigra were characterised by the greatest amount of variability. In fact, the large confidence interval characterising differences between the scan and rescan ROI QSM values (as highlighted by the Bland-Altman plots – RN_{RH}: CI = 47.71, RN_{LH}: CI = 37.62; SN_{RH}: CI = 41.18; SN_{LH}: CI = 43.49) were paired in all cases (except for SN_{LH}) with poor regression fits (RN_{RH}: m = 0.648, b = 29.65, RN_{LH}: m = 0.789, b = 19.571; SN_{RH}: m = 0.737, b = 29.184). Furthermore, the ICC value of the RN_{RH} (ICC = 0.735) was below the threshold for good repeatability (i.e., ICC < 0.75). These findings could be attributed to the small dimension of both structures, which could easily lead to biases in the extracted susceptibility measures due to partial volume effects (Rua et al., 2020; Lancione et al., 2022). In addition, the low reproducibility of red nucleus had already been noted by Santin and colleagues (Santin et al., 2017), who hypothesised as cause the suboptimal background field removal characterising that area. Due to their anatomical proximity, this could similarly affect the repeatability of the substantia nigra. Thus, the reconstruction pipeline used to derive susceptibility measures should be carefully considered and optimised when focusing on target areas of specific neurodegenerative conditions. This applies particularly well to Parkinson's disease (Guan et al., 2022), which is usually characterized by neurodegeneration of the substantia nigra.

The voxel-wise analysis was also restricted to all the above-mentioned gray matter nuclei using a binary mask of their union. Furthermore, it was iteratively repeated along a decreasing number of echo times (i.e., nTEs) ranging from 8 to 3. Overall, a trend of diminishing ICC values was displayed at lower nTEs. In particular, only QSM reconstruction derived using 8 and 7 echoes produced mean ICC values above the threshold fixed for good repeatability (i.e., 0.75 according to (Koo and Li, 2016)) across all nuclei. These were also the ones maximising the percentage of voxels characterised by an ICC greater than 0.75, over the whole binary mask. Moreover, when using nTEs lower than 7, the ICC metric provided negative results that indicate lack of interpretability for certain areas of the binary mask (Acosta-Cabronero et al., 2013). The amount of negative ICC scores became higher as we moved towards lower nTEs, suggesting increased difficulties in the assessment. As we investigated the nTEs impact on individual nuclei comprised within the binary mask, we found consistent results with respect to the ROI-based analysis conducted using 8 echoes. In fact, larger structures (i.e., PUT, GP, CN) showed the highest ICC values and good consistency across nTEs (i.e., ICC values remained above 0.75 across all nTEs, except for CN_{LH} at nTEs = 4). On the other hand, small subcortical brain nuclei such as amygdala, red nucleus and substantia nigra, despite maintaining acceptable ICC values (i.e., ICC > 0.75) at certain nTEs (see the “3.2. TE dependence” section for further details), demonstrated the greatest amount of variability. They were indeed characterised by performance drops, that affected different structures at different nTEs values. However, it should be noted that – overall – when using either 8 or 7 echoes it was possible to obtain ICC values > 0.75 for almost all structures in both brain hemispheres. This finding, coupled with results of the voxel-wise assessment, may be attributed to the lower signal-to-noise ratio (SNR) characterising QSM at lower nTEs. However, it should be noted that this association is not always accurate. According to Lancione and colleagues (Lancione et al., 2019), the highest SNR occurs when the TE of the imaging sequence equals the T2* value of tissues. At longer TE, though, results might become noisier. This holds particularly true for tissues characterised by short T2* relaxation and was further confirmed by the scan-rescan analysis performed on a single subject (see the *Supplementary Materials* for details), which revealed a trend of increasing SC1–SC2 differences at nTEs > 8. Therefore, it is important to carefully considered the TE-dependence of the SNR, especially for studies focusing on specific ROIs rather than the whole brain.

The results we obtained are supported by the number of subjects included in our analysis, which was greater when compared to the literature (Feng et al., 2018; Karsa et al., 2019; Rua et al., 2020; Salluzzi et al., 2022). Furthermore, the dataset was balanced in terms of sex (1:1 ratio between F and M) and age. This allowed us to remove most sources of potential bias that might have affected the local reliability of results. The only exception was represented by the subjects' head orientation with respect to the B_0 field, that is known to introduce a certain amount of variability in the final susceptibility estimates (Lancione et al., 2017). In this regard, we considered using a method called *Calculation Of Susceptibility through Multiple Orientation Sampling* (i.e., COSMOS) to reconstruct QSM (Liu et al., 2009). The algorithm can average out the orientation-dependent errors by acquiring multiple sets of images with different orientations. Nevertheless, its implementation is complex and severely time-consuming as it requires multiple MRI acquisitions. For this reason, it is not commonly used in clinical settings or longitudinal research studies, that represent the primary focus of our repeatability assessment. As a consequence, COSMOS was not involved in the analysis.

These considerations represent the main limitation of the present study, that concerns the use of a single reconstruction pipeline to derive the final QSM maps (spatial phase unwrapping: Laplacian based algorithm; background field removal: PDF; multi-echo combination: complex nonlinear fitting; susceptibility estimate: MEDI+0). Besides COSMOS, numerous algorithms can be adopted to perform the different processing steps and a former study attested they have an impact on the amount of reproducibility characterising results (Santin et al., 2017). Therefore, a careful evaluation should be conducted when deviating from the methods presented in this work.

5. Conclusions

Our study suggests that QSM is characterised by a good level of repeatability across repeated MRI scans. In addition, it shows that repeatability is influenced by the number of echo times used to derive the final susceptibility estimates, with more echoes generally resulting in more consistent outcomes. These findings are favourable as to the wide applicability of the present QSM acquisition/reconstruction protocol to longitudinal settings such as disease/treatment monitoring and rehabilitation trials. However, particular attention should also be devoted to the target brain structure under analysis, as smaller regions seem generally affected by a higher amount of variability. This indicates the need for careful methodological considerations, that must be tailored according to the neurodegenerative pathology of interest.

Data/code availability statement

The data presented in this study will be made available upon reasonable request to the authors due to ethical reasons.

Ethics statement

The study was conducted in accordance with the Declaration of Helsinki and approved by the local ethics committee. Informed consent was obtained from all subjects involved in the study.

Declaration of Competing Interest

The authors declare no conflict of interest. The funders had no role in the design of the study; in the collection, analyses, or interpretation of data; in the writing of the manuscript; or in the decision to publish the results.

Credit authorship contribution statement

Valentina Bordin: Conceptualization, Methodology, Formal analysis, Writing – original draft, Writing – review & editing. **Alice Pirastru:**

Methodology, Formal analysis, Writing – original draft, Writing – review & editing. **Niels Bergsland:** Methodology, Writing – review & editing. **Marta Cazzoli:** Data curation. **Giuseppe Baselli:** Conceptualization, Supervision, Writing – review & editing. **Francesca Baglio:** Conceptualization, Funding acquisition, Supervision, Writing – review & editing.

Data availability

Data will be made available on request.

Acknowledgements

We thank all participants for their time and Irene Incerti for the useful discussions on QSM reconstruction methods.

Funding

This research was funded by the Italian Ministry of Health (Neuroscience and Neurorehabilitation Network (RIN) - Ricerca Corrente Reti - RCR-2022).

Supplementary materials

Supplementary material associated with this article can be found, in the online version, at [doi:10.1016/j.neuroimage.2023.120272](https://doi.org/10.1016/j.neuroimage.2023.120272).

References

- Acosta-Cabrero, J., Williams, G.B., Cardenas-Blanco, A., Arnold, R.J., Lupson, V., Nestor, P.J., 2013. In vivo quantitative susceptibility mapping (QSM) in Alzheimer's disease. *PLoS One* 8 (11), e81093. doi:10.1371/journal.pone.0081093.
- Argyridis, I., Li, W., Johnson, G.A., Liu, C., 2014. Quantitative magnetic susceptibility of the developing mouse brain reveals microstructural changes in the white matter. *NeuroImage* 88, 134–142. doi:10.1016/j.neuroimage.2013.11.026.
- Clarke, W.T., et al., 2020. Multi-site harmonization of 7 Tesla MRI neuroimaging protocols. *NeuroImage* 206, 116335. doi:10.1016/j.neuroimage.2019.116335.
- Cornell MRI Research Group. Quantitative Susceptibility Mapping. Updated January 15, 2020. [Online]. Available: <http://pre.weill.cornell.edu/mri/pages/qsm.html>.
- Cronin, M.J., Wang, N., Decker, K.S., Wei, H., Zhu, W.-Z., Liu, C., 2017. Exploring the origins of echo-time-dependent quantitative susceptibility mapping (QSM) measurements in healthy tissue and cerebral microbleeds. *NeuroImage* 149, 98–113. doi:10.1016/j.neuroimage.2017.01.053.
- de Rochefort, L., et al., 2010. Quantitative susceptibility map reconstruction from MR phase data using Bayesian regularization: validation and application to brain imaging: Bayesian regularized solution for quantitative susceptibility mapping. *Magn. Reson. Med.* 63 (1), 194–206. doi:10.1002/mrm.22187.
- Desikan, R.S., et al., 2006. An automated labeling system for subdividing the human cerebral cortex on MRI scans into gyral based regions of interest. *NeuroImage* 31 (3), 968–980. doi:10.1016/j.neuroimage.2006.01.021.
- Du, G., et al., 2016. Quantitative susceptibility mapping of the midbrain in Parkinson's disease: nigral iron in PD. *Mov. Disord.* 31 (3), 317–324. doi:10.1002/mds.26417.
- Du, L., et al., 2018. Increased iron deposition on brain quantitative susceptibility mapping correlates with decreased cognitive function in Alzheimer's disease. *ACS Chem. Neurosci.* 9 (7), 1849–1857. doi:10.1021/acschemneuro.8b00194.
- Elkady, A.M., Sun, H., Wilman, A.H., 2016. Importance of extended spatial coverage for quantitative susceptibility mapping of iron-rich deep gray matter. *Magn. Reson. Imaging* 34 (4), 574–578. doi:10.1016/j.mri.2015.12.032.
- Emmerich, J., Bachert, P., Ladd, M.E., Straub, S., 2021. On the separation of susceptibility sources in quantitative susceptibility mapping: theory and phantom validation with an in vivo application to multiple sclerosis lesions of different age. *J. Magn. Reson.* 330, 107033. doi:10.1016/j.jmr.2021.107033.
- Fan, W., Wang, X., Zhang, X., Liu, M., Meng, Q., Chen, Z., 2020. Investigating optimal echo times for quantitative susceptibility mapping of basal ganglia nuclei in the healthy brain. *Curr. Med. Imaging Former. Curr. Med. Imaging Rev.* 16 (8), 991–996. doi:10.2174/1573405615666191219102044.
- Feng, X., Deistung, A., Reichenbach, J.R., 2018. Quantitative susceptibility mapping (QSM) and R_2^* in the human brain at 3T. *Z. Med. Phys.* 28 (1), 36–48. doi:10.1016/j.zemedi.2017.05.003.
- Frazier, J.A., et al., 2005. Structural brain magnetic resonance imaging of limbic and thalamic volumes in pediatric bipolar disorder. *Am. J. Psychiatry* 162 (7), 1256–1265. doi:10.1176/appi.ajp.162.7.1256.
- Fröhner, J.H., Teckentrup, V., Smolka, M.N., Kroemer, N.B., 2019. Addressing the reliability fallacy in fMRI: similar group effects may arise from unreliable individual effects. *NeuroImage* 195, 174–189. doi:10.1016/j.neuroimage.2019.03.053.
- Goldstein, J.M., et al., 2007. Hypothalamic abnormalities in schizophrenia: sex effects and genetic vulnerability. *Biol. Psychiatry* 61 (8), 935–945. doi:10.1016/j.biopsych.2006.06.027.

- Guan, X., et al., 2022. Altered brain iron depositions from aging to Parkinson's disease and Alzheimer's disease: a quantitative susceptibility mapping study. *NeuroImage* 264, 119683. doi:10.1016/j.neuroimage.2022.119683.
- Haacke, E., Liu, S., Buch, S., Zheng, W., Wu, D., Ye, Y., 2015. Quantitative susceptibility mapping: current status and future directions. *Magn. Reson. Imaging* 33 (1), 1–25. doi:10.1016/j.mri.2014.09.004.
- Hinoda, T., et al., 2015. Quantitative susceptibility mapping at 3 T and 1.5 T: evaluation of consistency and reproducibility. *Invest. Radiol.* 50 (8), 522–530. doi:10.1097/RLI.0000000000000159.
- Huang, W., Sweeney, E.M., Kaunzner, U.W., Wang, Y., Gauthier, S.A., Nguyen, T.D., 2022. Quantitative susceptibility mapping versus phase imaging to identify multiple sclerosis iron rim lesions with demyelination. *J. Neuroimaging* 32 (4), 667–675. doi:10.1111/jon.12987.
- Ippoliti, M., et al., 2018. Quantitative susceptibility mapping across two clinical field strengths: contrast-to-noise ratio enhancement at 1.5T: QSM across two clinical field strengths. *J. Magn. Reson. Imaging* 48 (5), 1410–1420. doi:10.1002/jmri.26045.
- Jenkinson, M., Smith, S., 2001. A global optimisation method for robust affine registration of brain images. *Med. Image Anal.* 5 (2), 143–156. doi:10.1016/S1361-8415(01)00036-6.
- Karsa, A., Punwani, S., Shmueli, K., 2019. The effect of low resolution and coverage on the accuracy of susceptibility mapping. *Magn. Reson. Med.* 81 (3), 1833–1848. doi:10.1002/mrm.27542.
- Koo, T.K., Li, M.Y., 2016. A guideline of selecting and reporting intraclass correlation coefficients for reliability research. *J. Chiropr. Med.* 15 (2), 155–163. doi:10.1016/j.jcm.2016.02.012.
- Lancione, M., et al., 2022. Multi-centre and multi-vendor reproducibility of a standardized protocol for quantitative susceptibility Mapping of the human brain at 3T. *Phys. Med.* 103, 37–45. doi:10.1016/j.ejmp.2022.09.012.
- Lancione, M., Donatelli, G., Cecchi, P., Cosottini, M., Tosetti, M., Costagli, M., 2019. Echo-time dependency of quantitative susceptibility mapping reproducibility at different magnetic field strengths. *NeuroImage* 197, 557–564. doi:10.1016/j.neuroimage.2019.05.004.
- Lancione, M., Tosetti, M., Donatelli, G., Cosottini, M., Costagli, M., 2017. The impact of white matter fiber orientation in single-acquisition quantitative susceptibility mapping. *NMR Biomed.* 30 (11), e3798. doi:10.1002/nbm.3798.
- Langkammer, C., et al., 2016. Quantitative susceptibility mapping in Parkinson's disease. *PLoS One* 11 (9), e0162460. doi:10.1371/journal.pone.0162460.
- Li, L., Leigh, J.S., 2004. Quantifying arbitrary magnetic susceptibility distributions with MR. *Magn. Reson. Med.* 51 (5), 1077–1082. doi:10.1002/mrm.20054.
- Li, W., Wu, B., Liu, C., 2011. Quantitative susceptibility mapping of human brain reflects spatial variation in tissue composition. *NeuroImage* 55 (4), 1645–1656. doi:10.1016/j.neuroimage.2010.11.088.
- Liu, M., et al., 2016. Assessing global and regional iron content in deep gray matter as a function of age using susceptibility mapping: global and regional iron content. *J. Magn. Reson. Imaging* 44 (1), 59–71. doi:10.1002/jmri.25130.
- Liu, T., Spincemaille, P., De Rochefort, L., Kressler, B., Wang, Y., 2009. Calculation of susceptibility through multiple orientation sampling (COSMOS): a method for conditioning the inverse problem from measured magnetic field map to susceptibility source image in MRI: COSMOS susceptibility imaging. *Magn. Reson. Med.* 61 (1), 196–204. doi:10.1002/mrm.21828.
- Liu, Z., Spincemaille, P., Yao, Y., Zhang, Y., Wang, Y., 2018. MEDI+0: morphology enabled dipole inversion with automatic uniform cerebrospinal fluid zero reference for quantitative susceptibility mapping. *Magn. Reson. Med.* 79 (5), 2795–2803. doi:10.1002/mrm.26946.
- Makris, N., et al., 2006. Decreased volume of left and total anterior insular lobule in schizophrenia. *Schizophr. Res.* 83 (2–3), 155–171. doi:10.1016/j.schres.2005.11.020.
- McGraw, K.O., Wong, S.P., 1996. Forming inferences about some intraclass correlation coefficients. *Psychol. Methods* 1 (1), 30–46. doi:10.1037/1082-989X.1.1.30.
- Murakami, Y., et al., 2015. Usefulness of quantitative susceptibility mapping for the diagnosis of Parkinson disease. *Am. J. Neuroradiol.* 36 (6), 1102–1108. doi:10.3174/ajnr.A4260.
- Naji, N., et al., 2022. Multisite reproducibility of quantitative susceptibility mapping and effective transverse relaxation rate in deep gray matter at 3T using locally optimized sequences in 24 traveling heads. *NMR Biomed.* 35 (11). doi:10.1002/nbm.4788.
- Nigri, A., et al., 2022. Quantitative MRI harmonization to maximize clinical impact: the RIN-neuroimaging network. *Front. Neurol.* 13, 855125. doi:10.3389/fneur.2022.855125.
- Patenaude, B., Smith, S.M., Kennedy, D.N., Jenkinson, M., 2011. A Bayesian model of shape and appearance for subcortical brain segmentation. *NeuroImage* 56 (3), 907–922. doi:10.1016/j.neuroimage.2011.02.046.
- Reichenbach, J.R., 2012. The future of susceptibility contrast for assessment of anatomy and function. *NeuroImage* 62 (2), 1311–1315. doi:10.1016/j.neuroimage.2012.01.004.
- Roy, D.S., Zhang, Y., Halassa, M.M., Feng, G., 2022. Thalamic subnetworks as units of function. *Nat. Neurosci.* 25 (2), 140–153. doi:10.1038/s41593-021-00996-1.
- Rua, C., et al., 2020. Multi-centre, multi-vendor reproducibility of 7T QSM and R2* in the human brain: results from the UK7T study. *NeuroImage* 223, 117358. doi:10.1016/j.neuroimage.2020.117358.
- Salluzzi, M., McCreary, C.R., Gobbi, D.G., Lauzon, M.L., Frayne, R., 2022. Short-term repeatability and long-term reproducibility of quantitative MR imaging biomarkers in a single centre longitudinal study. *NeuroImage* 260, 119488. doi:10.1016/j.neuroimage.2022.119488.
- Santin, M.D., et al., 2017. Reproducibility of R_2^* and quantitative susceptibility mapping (QSM) reconstruction methods in the basal ganglia of healthy subjects: R_2^* and QSM reproducibility in the basal ganglia of healthy subjects. *NMR Biomed.* 30 (4), e3491. doi:10.1002/nbm.3491.
- Snider, S.B., Bodien, Y.G., Bianciardi, M., Brown, E.N., Wu, O., Edlow, B.L., 2019. Disruption of the ascending arousal network in acute traumatic disorders of consciousness. *Neurology* 93 (13), e1281–e1287. doi:10.1212/WNL.00000000000008163.
- Sood, S., et al., 2017. Echo time-dependent quantitative susceptibility mapping contains information on tissue properties. *Magn. Reson. Med.* 77 (5), 1946–1958. doi:10.1002/mrm.26281.
- Spincemaille, P., et al., 2020. Quantitative susceptibility mapping: MRI at 7T versus 3T. *J. Neuroimaging* 30 (1), 65–75. doi:10.1111/jon.12669.
- Voelker, M.N., et al., 2021. The traveling heads 2.0: multicenter reproducibility of quantitative imaging methods at 7 Tesla. *NeuroImage* 232, 117910. doi:10.1016/j.neuroimage.2021.117910.
- Wang, Y., Liu, T., 2015. Quantitative susceptibility mapping (QSM): decoding MRI data for a tissue magnetic biomarker. *Magn. Reson. Med.* 73 (1), 82–101. doi:10.1002/mrm.25358.
- Wharton, S., Bowtell, R., 2015. Effects of white matter microstructure on phase and susceptibility maps: effects of Microstructure on Phase and QSM. *Magn. Reson. Med.* 73 (3), 1258–1269. doi:10.1002/mrm.25189.
- Wisnieff, C., Ramanan, S., Olesik, J., Gauthier, S., Wang, Y., Pitt, D., 2015. Quantitative susceptibility mapping (QSM) of white matter multiple sclerosis lesions: interpreting positive susceptibility and the presence of iron: iron and myelin content of MS lesions with MRI. *Magn. Reson. Med.* 74 (2), 564–570. doi:10.1002/mrm.25420.
- Zhou, D., Cho, J., Zhang, J., Spincemaille, P., Wang, Y., 2017. Susceptibility underestimation in a high-susceptibility phantom: dependence on imaging resolution, magnitude contrast, and other parameters: QSM estimation dependence on resolution, magnitude contrast, and other parameters. *Magn. Reson. Med.* 78 (3), 1080–1086. doi:10.1002/mrm.26475.